Available online at www.sciencedirect.com

ScienceDirect

journal homepage: http://www.elsevier.com/locate/acme

Original research article

A combined full-field imaging and metallography approach to assess the local properties of gas tungsten arc welded copper–stainless steel joints

R. Saranarayanan [a], A.K. Lakshminarayanan [a,*], B. Venkatraman [b]

[a] Department of Mechanical Engineering, SSN College of Engineering, Kalavakkam 603 103, Tamil Nadu, India
[b] Radiological Safety and Environmental Group, Indira Gandhi Centre for Atomic Research, Kalpakkam 603 102, Tamil Nadu, India

ARTICLE INFO

Article history:
Received 7 May 2018
Accepted 25 August 2018
Available online 27 November 2018

Keywords:
Gas tungsten arc welding
Copper
Stainless steel
Digital image correlation
Electron Backscatter Diffraction

ABSTRACT

The local material properties of gas tungsten arc welded (GTAW) C21000 grade copper alloy (Cu) to AISI 304 grade stainless steel (SS) joints using (ErNiCu-7) filler material are studied using a range of material characterization techniques. Electron Back Scattered Diffraction (EBSD) studies across the weld confirmed the relationships existing between the solidification modes (dendritic, planar) and their corresponding grain morphology in a high resolution. The SEM-Backscattered Electron Mode (BSE) integrated with Energy Dispersive Spectroscopy (EDS) analysis evidenced the local heterogeneous compositions across the dissimilar weld. The global and local mechanical performance of the weld joints are assessed using a conventional uniaxial tensile tests and full-field 2D-digital image correlation (DIC) respectively. The local material behaviour of the weld joint is in-line with the compositional and microstructural gradients. The weld joint has achieved the ultimate tensile strength (UTS) of 258 ± 14 MPa, which is very close to the strength of the Cu base metal (BM) and all the joints were fractured in the Cu-HAZ. Microhardness distributions measured using a spatially positioned indents found that the weld fusion zone (129.28 ± 19.22 HV) has higher hardness in compared to the Cu-BM (80.51 ± 2.58 HV).

1. Introduction

Material properties such as excellent thermal conductivity, high structural strength and good corrosion resistance have been required for materials employed in power generation and transmission process applications [1–4]. This is because, in these service environments, the material should have a high heat transmission rate with minimum heat loss but also it has to resist any form of corrosion in the service environment. However, it is not always possible to achieve all these properties in a single material. As a trade-off, a dissimilar combination of

* Corresponding author.
E-mail addresses: rsaranarayanan@gmail.com (R. Saranarayanan), LakshminarayananAK@ssn.edu.in, akln2k2@yahoo.com (A.K. Lakshminarayanan), bvenkat@igcar.gov.in (B. Venkatraman).
https://doi.org/10.1016/j.acme.2018.08.009
1644-9665/

materials may be used where one superior property can be provided locally in a structure whilst still utilizing the merits of the parent material elsewhere. In addition to this, emerging requirements for light-weight structures with optimized and varying performance and functionality have increased the scale of applications for multi-material structures [5]. Thus a need for joining materials with the different physical/thermal properties requires welding of dissimilar materials. One such example focused in this investigation is the combination of C21000 grade Copper alloy and AISI 304 grade Austenitic stainless steel. Copper has a Face Centred Cubic (FCC) crystal structure and high thermal conductivity properties (401 W/mK), so it has many applications in power generating industries because of its high electrical performance and excellent formability but it has an inferior corrosion resistance compared to stainless steel. In contrast, the Austenitic Stainless Steels are traditionally used as a structural materials in the nuclear, petrochemical and chemical industries due to their excellent corrosion resistance but they are not as good a conductor of heat as copper. Copper (Cu)–Stainless Steel (SS) joints are required in the nuclear power generating industries as one of the important components in the vacuum chambers for particle accelerators [6] and also in cryogenics [7] to utilize the high electrical conductivity of copper and high mechanical strength of the steel. To tailor the advantages of stainless steel with copper, a suitable welding process needs to be applied. But the wide differences in the properties of Cu and SS, such as melting point (Cu – 1085 °C, SS – 1400–1500 °C) and thermal conductivity (Cu – 401 W/mK, SS – 17–19 W/mK) makes the joining task much more challenging for any fusion welding processes. This is because the copper can conduct heat energy 10 times faster than steel which tends to dissipate the heat rapidly away from the weld zone making it difficult to achieve the melting point during fusion welding. In addition to that, copper has very limited solubility with steel in the liquid state and also the penetration of copper along the heat affected zone (HAZ) of the steel may lead to hot cracking [8]. However, a few investigations have been made to join this dissimilar combination (Cu to SS) via both fusion welding and solid-state welding processes. These feasibility studies have attempted to weld the Cu–SS dissimilar material joints using various welding techniques such as Electron Beam Welding (EBW) [7,9,10], Laser Beam Welding (LBW) [8,11–13], Explosive welding [14,15] and Friction Stir Welding processes [6,16–18]. However, it is clearly inferred that all the high energy fusion welding processes (EBW, LBW) are suffering from the major drawbacks and also more experimental difficulties have been involved in the solid state welding processes (Explosive, FSW) to join the Cu–SS material system.

It is vital to manufacture the dissimilar welds through a cost-effective welding process without compromising the quality and reliability of the welds. As the dissimilar welds have been enriched with microstructural and compositional gradients produced from two dissimilar materials, the locally varying properties of any dissimilar welds have to be assessed and correlated with the microstructures in a full-field scale [19]. Hence this investigation is attempted to clearly map the microstructural heterogeneities across the Gas Tungsten Arc Welded (Cu–SS) joints with the local mechanical behaviour through a range of material characterization techniques. Only two notable works have been carried to date for joining Cu–SS using the Gas Tungsten Arc Welding (GTAW) process. Sajjad et al. [20] investigated the feasibility study of copper to 304 stainless steel joints through GTAW process by using three different filler materials (316, Copper, Ni–Cu–Fe), and concluded that the joints fabricated with copper filler material led to the formation of sound weld zone without any macroscopic defects and also it had very high tensile strength compared to other filler materials. Chin-Chun Chang et al. [21] attempted the GTAW process in two dissimilar material combinations of Cu and SS (CuCrZr alloy-304 SS and OFHC-304SS) and successfully manufactured the joints without any major weld defects. However, all the above studies were not exercised through the detailed microstructural analysis and therefore the weld solidification behaviour and its corresponding elemental gradients across the fusion zone are not clearly evidenced. Additionally, the local material behaviour of the prominent weld zones such as fusion zone, HAZ and BM has not been assessed so far. Therefore, the detailed material characterizations exercised in this study will help to understand the local structure–property relationships of the dissimilar weld and to qualify the dissimilar GTAW (Cu–SS) welds for service with a high degree of confidence.

2. Experimental work

The as-received rolled sheets of C21000 grade copper (Cu) and AISI 304 grade austenitic stainless steel were machined to the required dimensions (200 mm × 75 mm × 2 mm) in a precision cutting machine with an appropriate cutting fluid supplied as a coolant. The chemical compositions of these sheets and the filler material are presented in Table 1. To achieve an adequate penetration of the filler metal during the welding process, a ''V'' Shaped groove with 60° included angle was machined at the sheet edges. Before welding process, the butting surface of the sheets was thoroughly cleaned with a lower grit silicon abrasive papers followed by cleaning with acetone to eliminate the surface oxide contaminations. The ErNiCu-7 was down-selected as the filler material as both the copper alloy and nickel filler materials were reported as the successful candidates in joining the Cu to SS via arc welding process [20,22]. A typical GTAW experimental set-up used to manufacture the GTAW (Cu–SS) joints is shown in Fig. 1.

Table 1 – Chemical compositions of the base materials and filler metal (in wt%).

Material	Mn	Si	P	S	Cr	Ni	Mo	Cu	Fe	Zn
Base Metal (AISI 304)	0.945	0.302	0.036	0.003	18.142	8.13	0.3	–	72.142	–
Base Metal (C21000 Copper)	0.002	0.003	0.006	0.009	0.006	0.023	–	93.621	0.010	6.320
Filler Metal (ERNiCu-7)	4	1.25	0.02	0.015	–	69	–	23.215	2.5	–

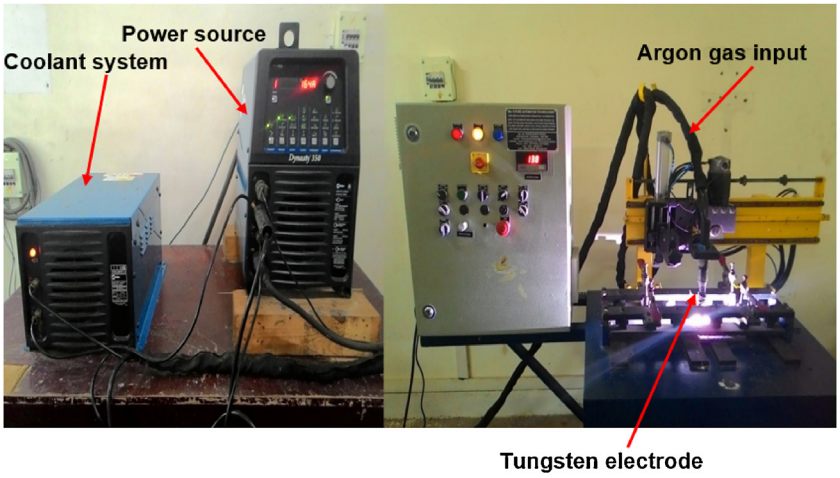

Fig. 1 – GTAW experiment set-up (Make: Miller Dynasty-350).

In advance to the welding process, the copper plate was preheated to 500 °C to prevent excessive heat dissipation through a high thermal conductivity characteristics of the copper [8,22]. Because of this pre-heat treatment, the arc was positioned exactly on the interface without any offsets to provide an uniform heat distribution to both base materials. During the manufacturing process, the filler material was loaded with an automatic feed head and the welding torch was positioned in normal to the welding direction at a standoff distance of 1 mm. To optimize the key process parameters, the welding current was varied from 80 to 195 A whilst the welding speed was maintained constant at 80 mm/min. These parameters were chosen based on the inference from the previous studies [20–22]. In additional to a single weld pass, a few joints were subjected to an additional pass (root pass) to enhance the penetration along the surface and root of the joints. The outcomes obtained from four different experimental trials are listed in Table 2. At very high welding current (195 A, 145 A), the joints have suffered from weld defects such as macro-level distortion and abnormal filler material deposition. This is because of the solidification turbulence caused by the excessive melting of copper. It is noteworthy that, the experimental trials conducted at very low welding current (80 A) resulted in insufficient weld penetration along the root side of the weld. However, the joint which was manufactured at 95 A does not exhibits any macro-level distortion and major weld defects. Therefore, the GTAW (Cu–SS) joint (as shown in Fig. 2a) manufactured using 95 A and 80 mm/min with other process parameters listed in Table 3 is considered for further material characterizations.

Table 2 – Experimental trials and its corresponding outcomes.

Welding current (A)	Welding speed (mm/min)	Macrograph	Outcomes
195	80	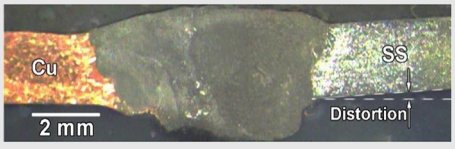	Weld macro level distortion, excessive melting and penetration
145	80	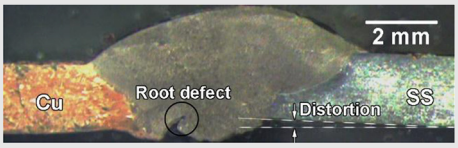	Weld macro level distortion, defect at the Cu side root
95	80		No macroscopic defects
80	80	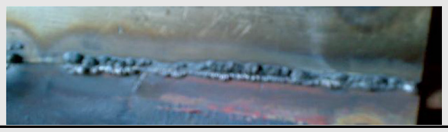	Improper fusion at the root

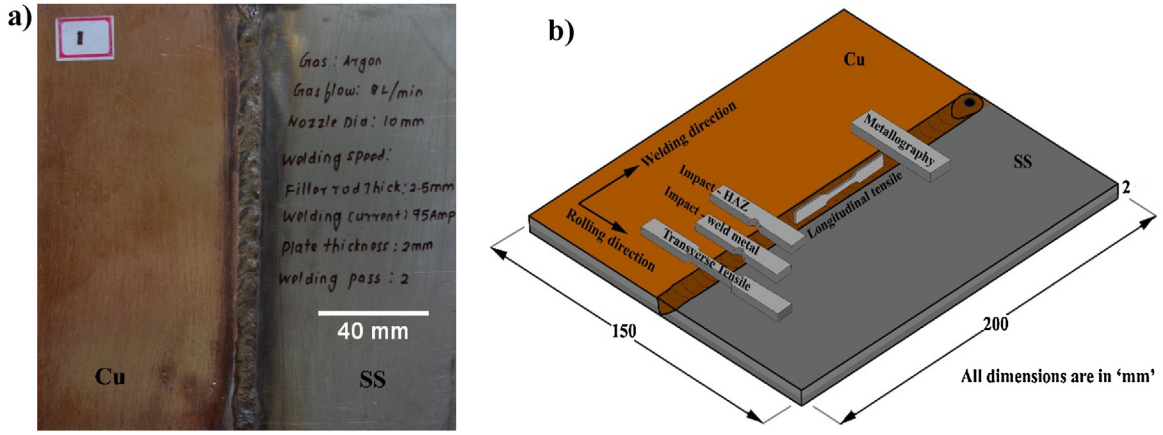

Fig. 2 – (a) A typical GTAW (Cu–SS) joint. (b) Specimens extraction scheme for various material characterizations.

The scheme for extracting the test specimens from the welded joint is shown in Fig. 2b. All the transverse tensile specimens were machined according to ASTM E8M-16a, sub-size standard [23] using wire cut Electric Discharge Machine. To achieve an uniform cross-section across the gauge section, all the extra filler material deposited on the fusion zone of the transverse tensile specimens was removed using rotary surface grinder. To evaluate the transverse tensile properties of the GTAW welds, three sub-size tensile specimens of standard dimensions (Fig. 3a) have tested to failure. The 2D-Digital Image Correlation (DIC) experiment was performed in the Instron servo-hydraulic 100 kN capacity testing machine in the position control mode with the displacement rate of 0.5 mm/min using the standard DIC test procedures. To achieve the varying grey levels on the specimen surface, the black speckled patterns required for the DIC experiments was created using an aerosol spray paint on a white painted background specimen. The DIC system consists of 8-bit CMOS camera (Marlin-F131) having a spatial resolution of 1280 × 1024 pixels fitted with the Nikon 50 mm focal length lens. Through these optics, the images were captured at the spatial resolution of 30 pixel/mm and the specimen surface was maintained normal to the sensor axis to avoid the out-of-plane deformations. An adequate illumination was provided with a pair of LED lights and all the images were recorded at a frequency of 5 Hz during the DIC experiments. Load values for each image being captured were recorded using a separate ADC channel data acquisition system. All the recorded images were processed through the DIC data correlation software (VIC-2D) using the subset size and step size of 29 × 29 pixels, 5 pixels respectively to evaluate the deformation field and full-field strain maps in the local weld zones. An ASTM E23-12c [24] guidelines was followed for preparing the impact toughness specimens. Impact toughness specimens have tested at room temperature using pendulum type Charpy impact testing machine. The schematic sketch of the impact specimens manufactured is shown in Fig. 3b.

The microhardness variations were measured across the cross-section of the weld in the fine polished specimen using microhardness tester (Mitsutoyo-Japan, Model: HV-112). As per ASTM E384-17 [25] standard, the distance maintained between

Table 3 – GTAW optimized process parameters.

Parameters	Value
Tungsten electrode diameter (mm)	2
Welding current (A)	95
Voltage (V)	20
Shielding gas	Argon
Gas flow rate (l/min)	8
Stand-off distance (mm)	1
Weld torch inclination	0°
Welding speed (mm/min)	80
Plate thickness (mm)	2
Filler diameter (mm)	2.5

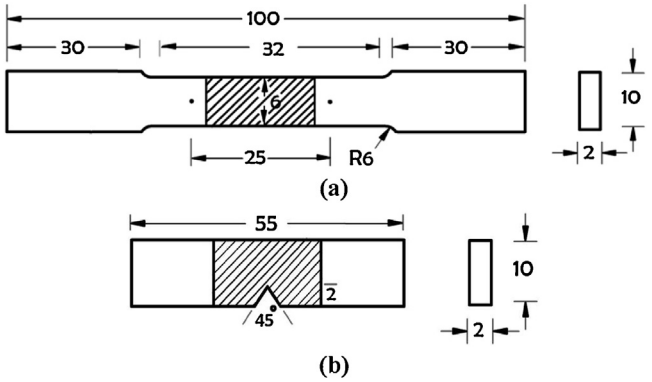

Fig. 3 – Sample dimensions used for (a) tensile test, (b) impact test (all dimensions are in 'mm').

the indents was 0.1 mm and all the indents were placed at a load of 50 g with a dwell time of 15 s for microhardness measurements. For metallography analysis, the specimen was subjected to different grades of silicon abrasive papers, diamond compounds (particle size: 6 μm, 1 μm) and final polishing was performed with the Nap polishing cloth suspended with a 0.04 μm colloidal silica solution. Macrostructural characteristics of the specimen were captured by stereomicroscope under a low magnification (10×). For microstructural analysis, the specimens were etched with 25 g $FeCl_3$ + 25 ml HCl + 100 ml H_2O solution for the duration of 10–15 s to observe the microstructural features using an optical microscopy (MEJI, Japan; model MIL-7100) integrated with image analyzing software (Metal Vision). For more detailed microstructural analysis of the joints, the Field-emission Scanning Electron microscopy (JEOL, Model: 6500F) was used at different magnifications in Secondary and Backscattered electron mode (SEI and BEI) at an accelerating voltage of 15 kV. For elemental analysis, Energy Dispersive X-ray Spectroscopy (EDS) integrated with the SEM was used to map the elemental composition distributed in the vicinity of welds. An EBSD (HKL Nordlys Detector with HKL channel 5 Flamenco software) characterization was carried out at an accelerating voltage of 20 kV, Probe current of 17 nA with a step size of 1 μm to measure the grain size as well as its relative orientations. All the EBSD scanned datasets were post-processed by the Tango Map software for further quantitative analysis such as grain boundary distributions, grain misorientations and grain size statistics.

3. Results and discussion

3.1. *Macrostructure*

Fig. 4 shows the sequentially stitched macrographs across the cross-section revealing various local weld zones of the GTAW (Cu–SS) joint. The GTA welded (Cu–SS) joint using ERNiCu-7 filler material produced a complete penetration, uniform weld bead without any distortion. Additionally, the weld interfaces are clearly identified and the joint is completely free from macroscopic defects (cracks, pores) and other volumetric defects (slag and inclusions).

3.2. *Microstructural characterizations*

Fig. 5a–i shows the optical micrographs captured at various zones across the weld of the GTA welded Cu–SS joint as located in the macrostructure. Fig. 5a represents the Cu base metal which exhibits large equiaxed copper grains with annealing twins. A significant grain growth with fully grown annealing twins are observed in the Cu-HAZ compared to the Cu-BM as shown in Fig. 5b. Although the copper has very high thermal conductivity, these grain growths were due to the high heat input and low welding speed adopted during the GTAW process [26]. Thus the convective flow of heat from the fusion zone to the Cu-BM through the Cu side interface was responsible for the grain growth in the Cu HAZ. Both Cu (Fig. 5c) and SS weld interfaces (Fig. 5g) are clearly observed in the optical micrographs. The copper interface has the wavy structure (Fig. 5c) in contrast to a sharp interface and also it is totally free of any microscopic defects such as porosity and hot cracking. Although Cu has very low solubility in the Fe, the presence of nickel in the filler material could extend the solubility level and thus the formation of weld defects was eliminated along the interface [22]. All the aforementioned microstructural features towards the Cu have indirectly confirm the complete metallurgical bonding between the ErNiCu-7 filler material and the Cu-BM. Fig. 5d–f shows the complex composite structure of the fusion zone where it has the copper matrix reinforced with the steel globules. It is noteworthy that some heterogeneously nucleated steel globules were not completely solidified into the dendrites. Additionally, the fusion zone has the mixture of cellular and dendritic solidification modes with the solidified distinct subgrain boundaries. This is because of the local temperature, solidification and composition gradients of the fusion zone. Due to the constitutional supercooling achieved via dendritic solidification process, more equiaxed dendrites are randomly populated in the direction normal to the weld interface and all the equiaxed dendrites have tree-like features with the primary dendrite arm and branches of the secondary dendrite arms. These equiaxed dendritic structures have high resistance to hot cracking during the solidification of the weld metal [27]. Although the directional growth of these dendrites is widely depended on the direction of convective heat flow and thermal conditions of the solidification process, however the final grain structure of the weld metal could be affected by the base material grains [26]. All the microstructural features observed across the fusion zone indicates the complete penetration of ErNiCu-7 filler material into the fusion zone and there is no evidence of any major weld defects. The continuous grain boundaries from the fusion line towards SS clearly demonstrate the behaviour of epitaxial grain growth and this growth is extended up to a few hundred μm towards the fusion zone as shown in Fig. 5g. This epitaxial grain growth formation is

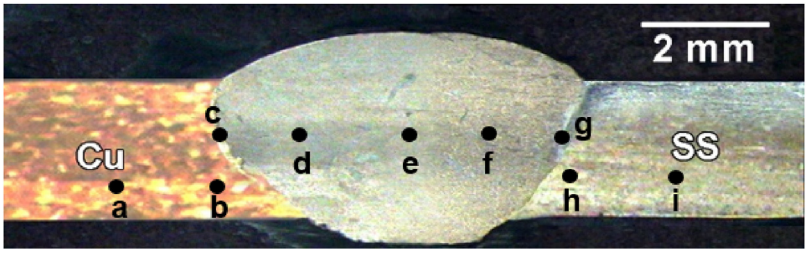

Fig. 4 – Cross-sectional Macrostructure of the GTAW (Cu–SS) joint showing various weld zones (a) base metal (BM)-copper, (b) HAZ-copper side, (c) copper–weld interface, (d)–(f) fusion zone, (g) weld–stainless steel interface, (h) HAZ-stainless steel side, and (i) BM-stainless steel.

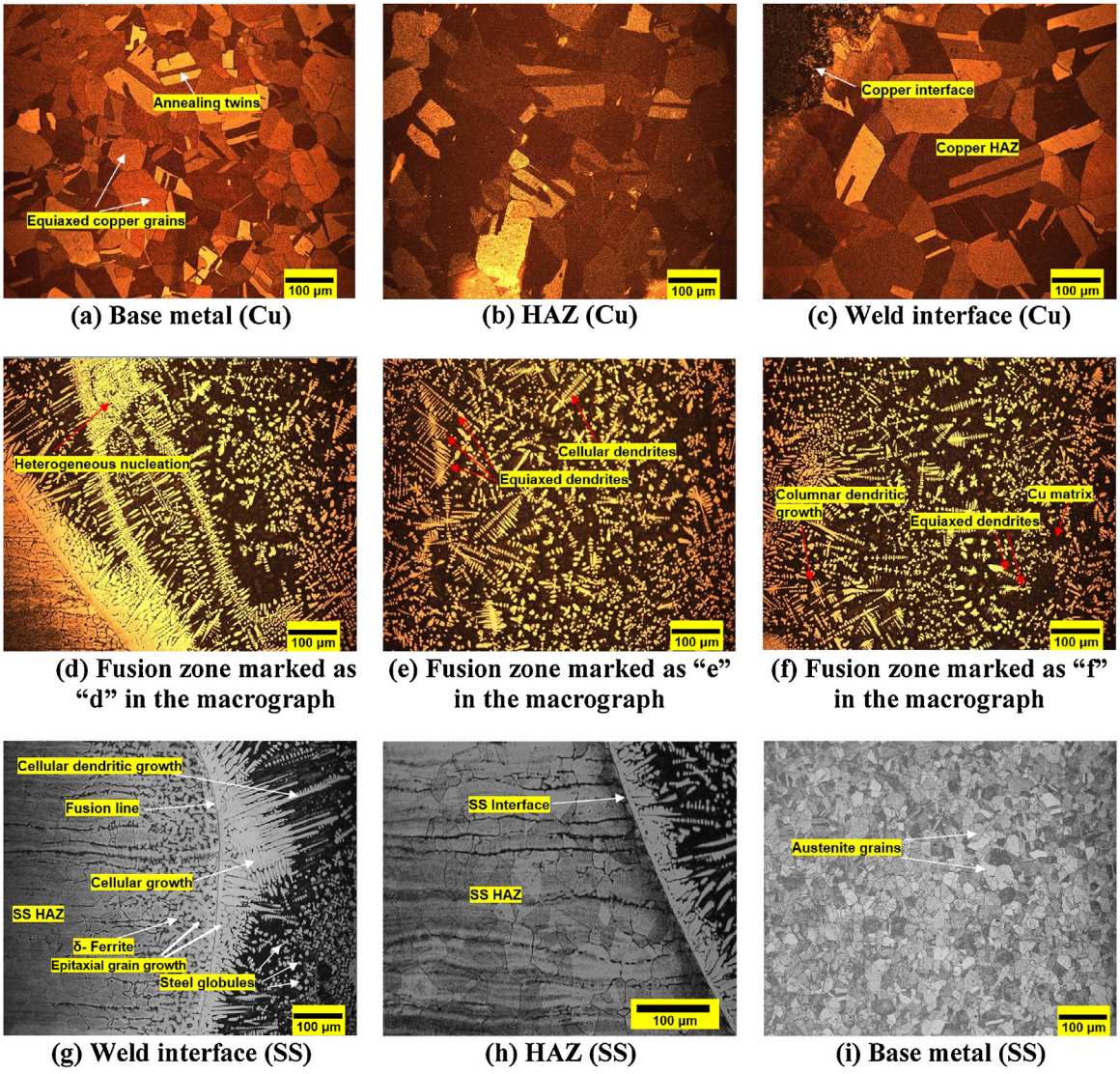

Fig. 5 – Optical micrographs of the GTAW (Cu–SS) joint made using ErNiCu-7 filler material (imaged at the magnification 200×, BF mode).

because of the similar chemical compositions and crystal structures (FCC) of Cu and the filler material as observed elsewhere [22,26]. The region close to the SS HAZ (Fig. 5g) has δ-ferrites (BCC) within the austenite matrix (FCC) produced from the allotropic phase transformations of the SS. The region covered by these dual phases (δ-ferrite + austenite) is categorized as unmixed zone (UMZ) where the filler material was not completely diffused with the base metal [27]. Fig. 5i shows the complete equiaxed austenite grains with annealing twins. In contrast to this microstructure, a coarse grain structure is clearly noted in the HAZ after a few μm distance from the SS interface (Fig. 5h).

Fig. 6a–d shows the high-resolution SEM micrographs captured at the weld interfaces and fusion zone of the GTAW (Cu–SS) joint. The SEM-BSE image (Fig. 6a) shows the compositional differences existing between the Fe globules and copper matrix, where the higher atomic number (Z_{Cu} = 29) and lower atomic number (Z_{Fe} = 26) elements are represented with the bright and dark features respectively. From this result, it is confirmed that Fe globules in the form of dendrites are densely populated on the copper matrix at the fusion zone. As observed in the optical micrographs, the epitaxial grain growth with delta ferrites (BCC) are well noticed at the SS interface (Fig. 6b). This is because, 304 stainless steel primarily solidify as delta ferrite (δ-Fe) and then transform to austenite (γ-Fe) upon cooling below its solidification temperature [26]. The solidification behaviour across the fusion line has a typical cellular grain growth, however due to high solidification rates and very low-temperature gradients of the fusion zone, the solidification behaviour has transformed into the mixture of columnar and equiaxed dendrites. Copper generally dissipates significant amount of heat away from the fusion zone due to its high thermal conductivity, therefore this phenomenon has heavily melted the Fe compared to the Cu and led to extensive supercooling and promoted the heterogeneous nucleation in the form of Fe globules on the copper matrix. Moreover, the heterogeneous

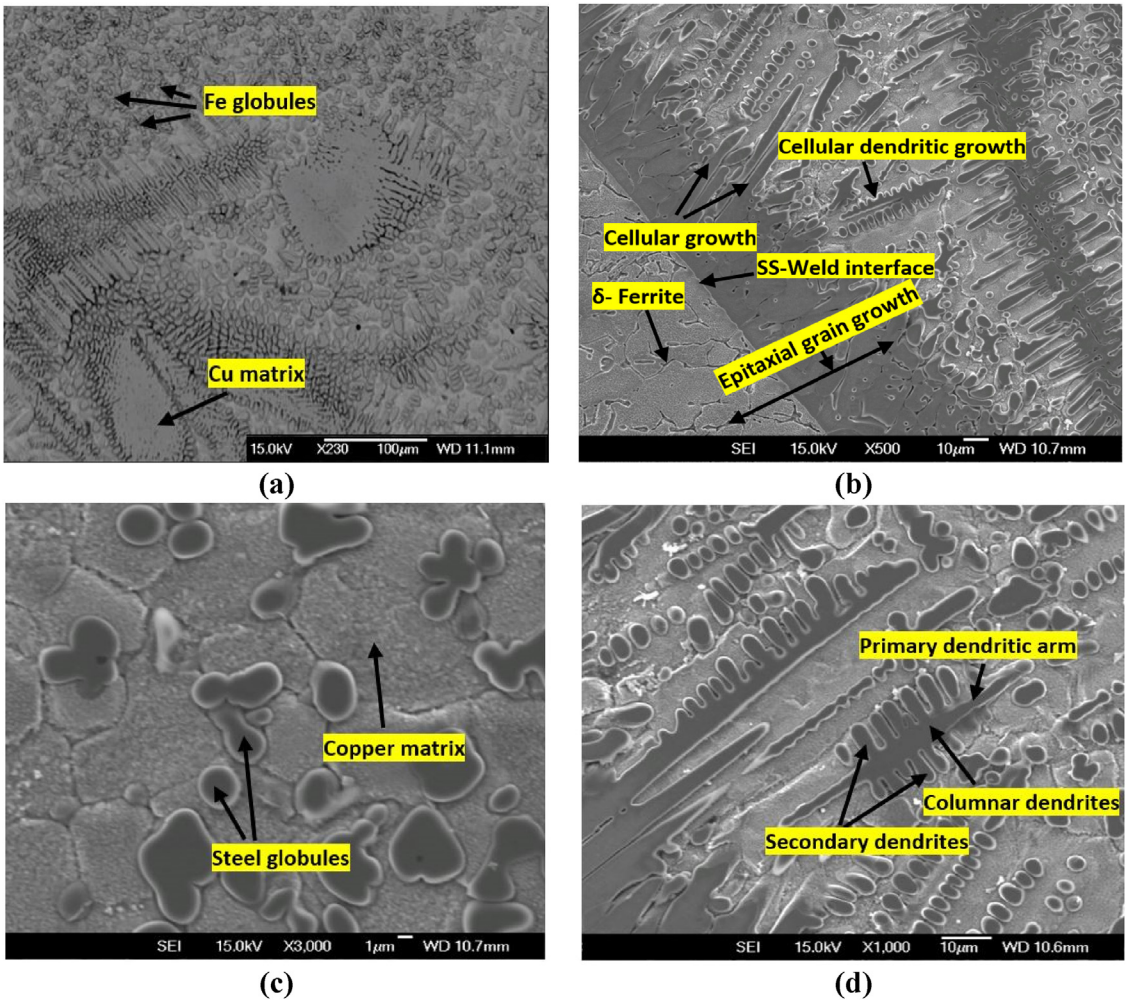

Fig. 6 – SEM micrographs across the fusion zone of the GTAW (Cu–SS) joint.

nucleation also created the steep concentration gradients and therefore more Fe nucleation spots with the solidified sub-grain boundaries are produced in the copper matrix as shown in Fig. 6c. The fusion zone had more supercooling effects received from the ErNiCu-7 filler material compared to the weld interface, therefore some long columnar grains have transformed into the equiaxed dendrites with primary and secondary dendritic arms (Fig. 6d). The size and spacing of these dendrites is totally controlled by the solidification parameters such as solidification modes, temperature gradients and solidification rates [26]. Furthermore, all the dendrites are aligned normal to the fusion line as shown in Fig. 6d. Thus the combined effects received from the constitutional supercooling as well as the composition and solidification gradients in the fusion zone have produced the complex dendritic solidification structure across the fusion zone. All the SEM findings are in good agreement with the optical micrographs and additionally it demonstrates the perfect bonding achieved between the BMs (Cu and Fe) and filler material.

3.3. *Elemental mapping analysis*

Fig. 7 shows the SEM images and its corresponding EDS elemental maps derived from the zones across the weld interfaces and fusion zone of the dissimilar joint. The corresponding qualitative EDS elemental analysis (in atm%) obtained from these EDS maps are shown in Table 4. In addition to Fe and Cu as the major elements, the presence of other elements such as C, O, Cr, Mn, Ni and Zn are also evident in the fusion zone and weld interfaces. All these elements are found as the minor alloying elements for both stainless steel and copper BM. As confirmed elsewhere [12,22], the presence of thermodynamically stable intermetallic phases is not evident in the fusion zone (as shown in Fig. 7b). Although the GTAW process has always been performed in an inert gas atmosphere to avoid the oxidation process, however the oxidation cannot be completely avoided if there is any highly reactive external environmental conditions [22]. Additionally, the oxygen ($Z = 8$) generally has very low resistance to penetrate into the grain boundary of the steel/copper and therefore the diffusivity of this element is very high. Thus, the presence of oxygen was noticed in the weld interfaces and fusion zone. From Fig. 7a, it is inferred that SS–weld interface has a significant amount of Fe (49.79 atm%) with small quantity of Cu (20.92 atm%). This shows that Cu elements not completely diffused towards the SS during the solidification process due to the high thermal conductivity of the Cu.

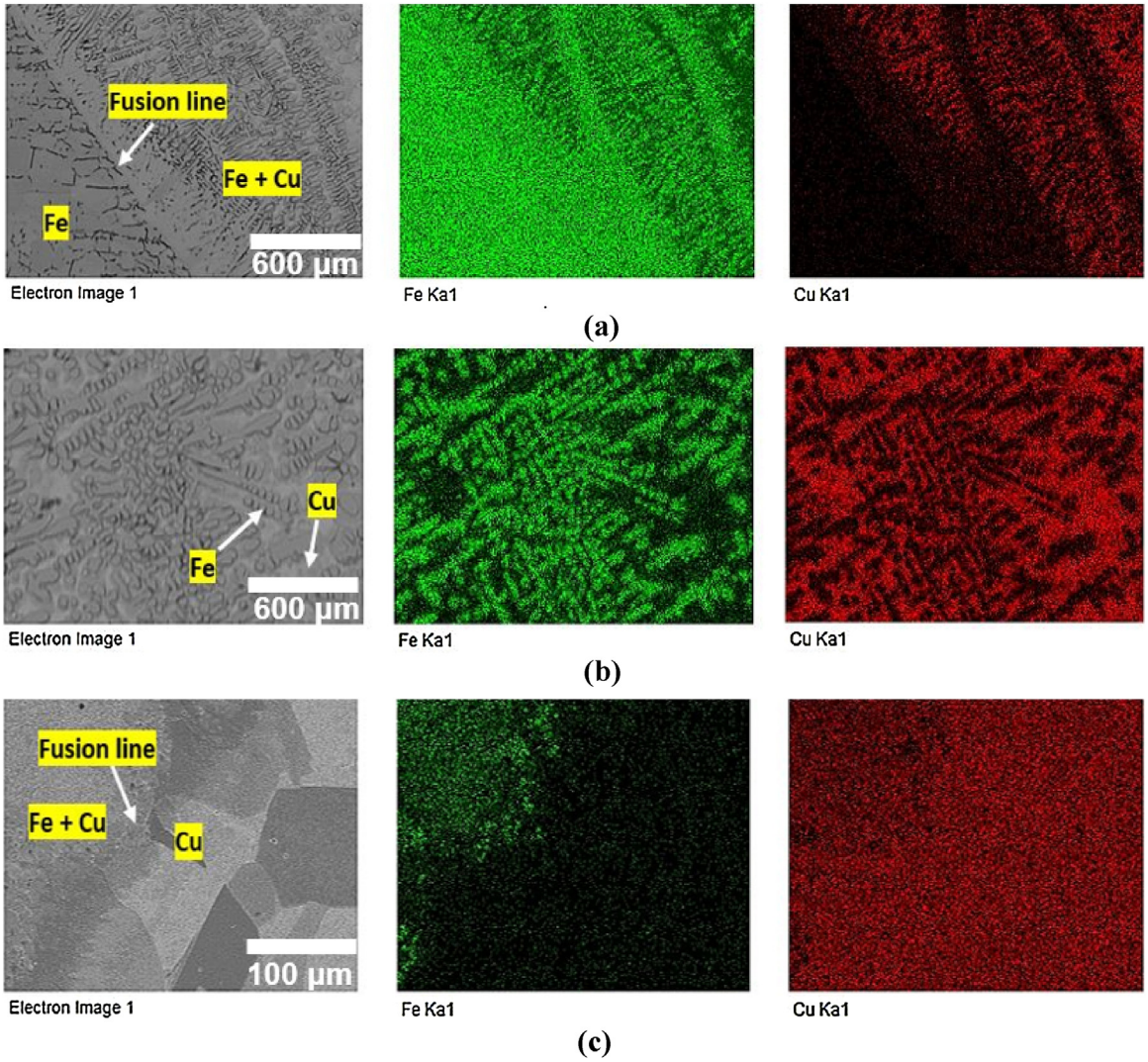

Fig. 7 – SEM-EDS micrographs at different zones of the GTAW (Cu–SS) joint (a) SS–weld interface, (b) fusion zone, and (c) Cu–weld interface.

The presence of high chromium content (12.67 atm%) in the SS interface represents the high corrosion resistance capability of the stainless steel. EDS mapping in the fusion zone demonstrates (Fig. 7b) the rich mixture of Cu (45.4 atm%) and Fe (27.41 atm%), where all the columnar dendrites are mapped as Fe and the fusion matrix is clearly mapped as copper. Furthermore, the fusion zone has significant amount of nickel (12.20 atm%) composition obtained from the diffusion of filler material during the welding process. This higher proportion of nickel in the fusion zone could extend the solubility of Cu in Fe and therefore it can avoids the microsegregation of Fe and Cu as found elsewhere [12]. From this map, it is also observed that all the columnar dendrites are clearly embedded in the Cu matrix and also the BMs have diffused well with the filler material without any microscopic defects.

Although the fusion zone has the rich mixture of Fe and Cu, the proportion of Cu distribution is significantly higher than the Fe. This is because of the Cu diffused from the filler material in addition to the Cu-BM has made the fusion zone enriched with more Cu than the Fe. Fig. 7c shows the EDS maps from the region between the fusion zone and Cu–weld interface, where the Fe migration towards Cu is clearly evident. It is noteworthy that a sharp fluctuation in elemental distribution of Fe and Cu is observed at the partially melted

Table 4 – SEM-EDS element analysis (in atm%).

Region	O Kα	Cr Kα	Mn Kα	Fe Kα	Ni Kα	Cu Kα	Zn Kα
SS/weld interface	5.88	12.67	1.06	49.79	9.68	20.92	–
Fusion zone	6.74	7.36	0.89	27.41	12.20	45.4	–
Cu/weld interface	5.66	1.08	1.27	9.09	8.43	69.4	5.07

zone (close to the Cu–weld interface) due to the local composition and temperature gradients activated by the constitutional liquation mechanism. All these EDS maps captured at the weld interfaces confirmed a perfect bonding between the BMs (Cu and Fe) and filler material. Hence all the aforementioned findings from the SEM-EDS maps clearly proves the heterogeneous compositions of the fusion zone and composite mixtures (Fe and Cu) at the Cu–weld interface of the joint.

3.4. *EBSD microstructural analysis*

EBSD Image quality (IQ) map, IQ map with Low angle grain boundaries (LABs) and High angle grain boundaries (HABs) and Inverse pole figure (IPF) of the GTAW (Cu–SS) weld zones are shown in Fig. 8. As both the Cu-BM and weld metal have more homogeneous material compositions, the transition of microstructure from the weld metal to the Cu–weld interface is apparently more gradual compared to SS–weld interface. Therefore in this investigation, the Cu–weld interface region was not considered for the EBSD analysis. To calculate the proportion of HABs and LABs from the EBSD scanned datasets, a cut-off angle of 2° was applied to eliminate spurious grain boundaries and to minimize the grain orientation noise in the misorientation distributions. From the statistics data obtained from the grain maps, a general misorientation criterion was applied to differentiate the (LABs) from the (HABs). All grains with a misorientation angle in the range of (2°–15°) were mapped as the (LABs) and the remaining grains (>15°) were mapped as the (HABs). Inverse pole figure (IPF) orientation components of the EBSD maps represent the direction of the grain orientations such as ⟨1 0 0⟩, ⟨1 1 0⟩, ⟨1 1 1⟩ with respect to the plane normal of the weld zones are also shown along with the IQ map (Fig. 8). Fig. 8a shows the equiaxed copper grains with annealing twins exhibited by the copper base material. From Fig. 8d, it is clearly noticed that the Cu-HAZ has large size grains compared to the Cu-BM. Fig. 8g reveals the austenitic grains of the stainless steel base material. The SS

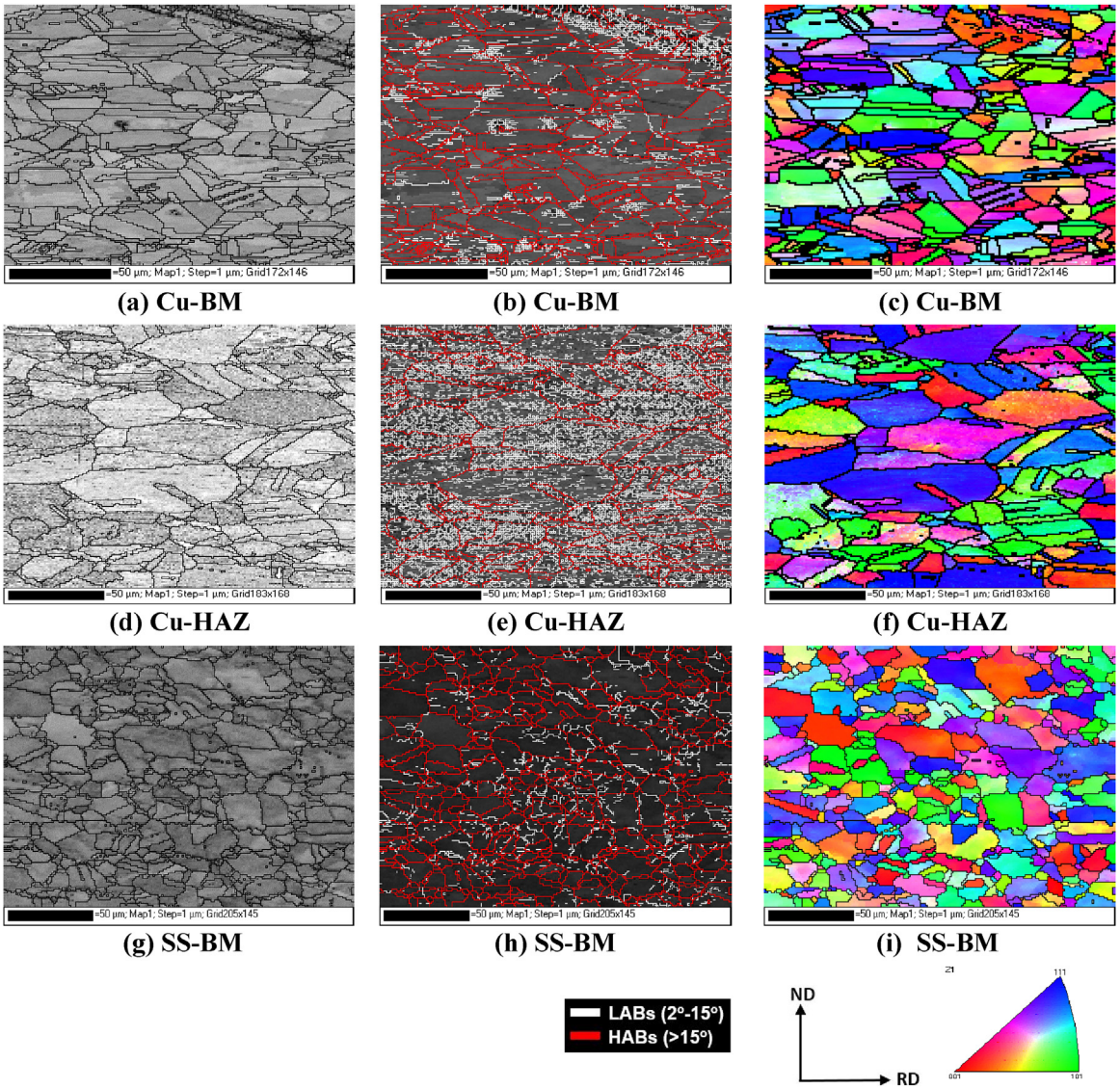

Fig. 8 – (a) EBSD image quality (IQ) map, (b) IQ map with LABs and HABs, (c) IPF of the Cu-BM, (d) IQ map, (e) IQ map with LABs and HABs, (f) IPF of the Cu HAZ, (g) IQ map, (h) IQ map with LABs and HABs, and (i) IPF of the SS-BM.

HAZ (Fig. 9b) has significant quantity of coarse grains compared to its BM.

As the base materials (Cu and SS) were remote from the fusion zone, many Cu and SS base material grains have more random grain orientations. All these base materials (Cu and SS) and its corresponding HAZ grain characteristics derived via EBSD are consistent with their optical micrographs. Fig. 9 shows the EBSD IQ and IPF map of the region (SS–weld interface) as located in the SEM micrograph (Fig. 9a). From this, it is evident that all the SS grains located very close to the fusion line had abnormal grain growth with the average grain size of 16.6% higher than the grains located in the HAZ. Fig. 10 shows the EBSD IQ and IPF map of the fusion zone as located in the SEM micrograph (Fig. 10a). The fusion zone has the mixture of coarse grains (Cu) with a major scale of equiaxed fine grains (SS). From the SEM-EDS maps (Fig. 7a,b), these equiaxed fine grains are already determined as SS globules nucleated through the dendritic solidification process. Although the fusion zone had significant amount of heat during the welding process, the majority of the weld heat was dissipated via filler metal (ERNiCu-7) and Cu-BM due to their high thermal conductivity. Thus from the EBSD micrographs of the fusion zone, it is clearly inferred that due to insufficient heat, more quantity of steel globules embedded in the copper matrix solidified into an equiaxed fine grains without forming a dendrites.

Grain misorientation angle distributions of the GTAW (Cu–SS) weld zones are also mapped in Fig. 8. Generally, LAGBs generated between a large size grain and its corresponding interior grain (or sub-grains), but the formation of HAGBs are usually between the two-grain boundaries [29,30]. Both Cu and SS base materials have 63.24% and 74.12% of HABs respectively. The LABs and HABs proportions of the SS HAZ is almost equivalent to the SS-BM. However due to more absorption of heat in the Cu-HAZ, in addition to large Cu grains generated from the heat source, this zone also has the significant branches of sub-grains as shown in Fig. 8e. Because of the microstructure turbulence caused by these sub-grains, the LABs (75.51%) and HABs (24.48%) counts of this zone are converse to its BM. Fig. 11 shows the grain size distribution around various zones of the GTAW (Cu–SS) weld and the grain size statistics is shown in Table 5. The copper base material has a wide range of grain sizes with an average grain size of 38.47 ± 5.48 μm and the stainless steel base material has the average grain size of 31.17 ± 6.03 μm. Average grain size of the Cu and SS HAZs were evaluated as 42.99 ± 4.71 μm and 39.20 ± 5.07 μm respectively. The weld fusion zone has the average grain size of 13.72 ± 7.47 μm. This more scatter in the grain size is due to the dense population of fine SS globules on the coarse copper matrix. As confirmed in the EBSD micrographs, among all the weld zones, the SS–weld interface zone has the highest average grain size of 52.98 ± 3.92 μm. Although the fusion zone had significant amount of heat during the welding process, the majority of the heat input was dissipated via high thermal conductivity copper grains densely populated in this zone. Hence, high cooling rate received from the copper has significantly controlled the grain growth in fusion zone (average grain size: 13.72 ± 7.47) and led to formation of dendritic solidification as shown in Fig. 10a. However, the solidification mode observed along the SS interface is widely varying in compared to the fusion zone. Due to the absence of copper in the SS interface, the cooling

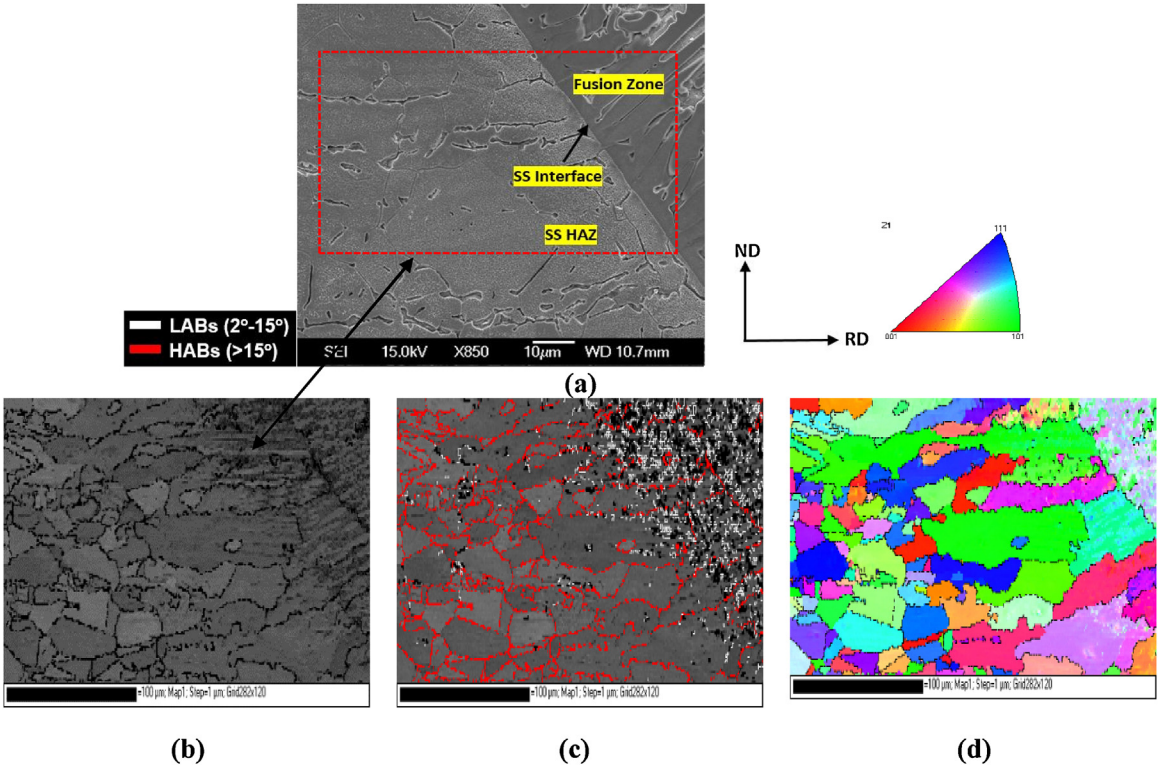

Fig. 9 – (a) SEM micrograph, -ROI for EBSD, (b) IQ map, (c) IQ map with LABs and HABs, (d) IPF of the SS–weld interface.

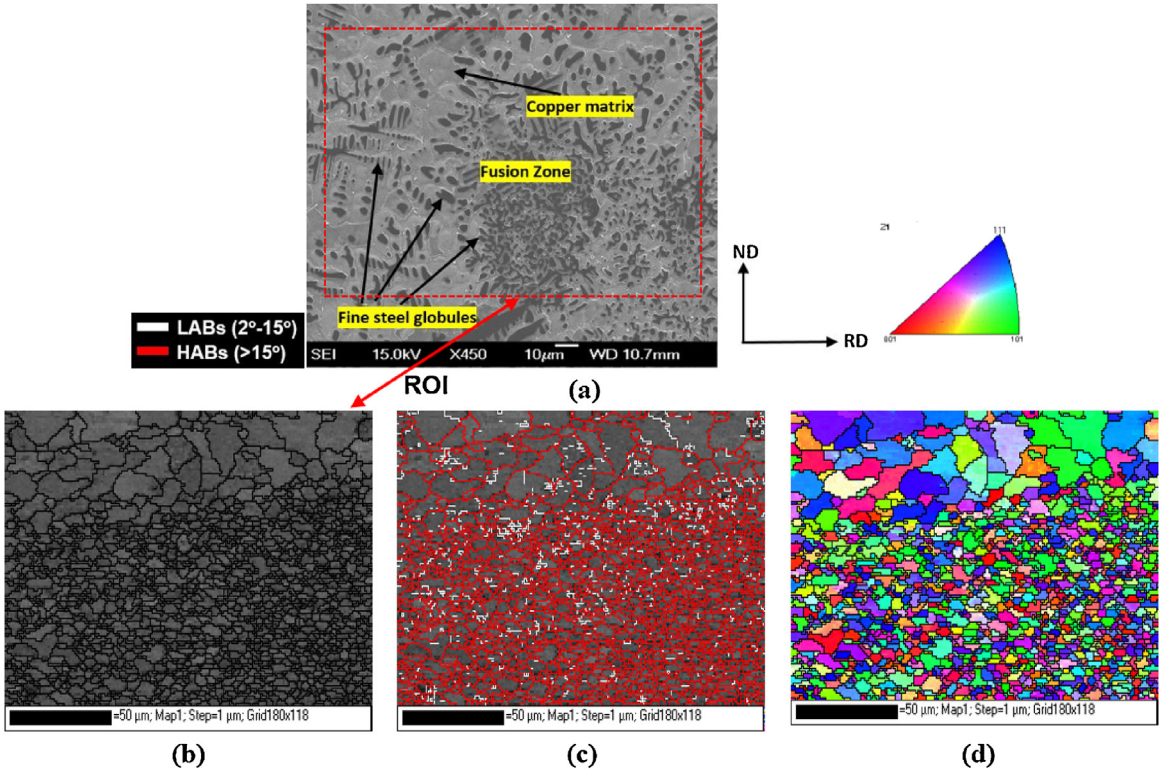

Fig. 10 – (a) SEM micrograph with ROI used for EBSD, (b) IQ map, (c) IQ map with LABs and HABs, and (d) IPF of the fusion zone.

rate during weld solidification was significantly reduced and led to formation of planar solidification with much coarser grains (average grain size: 52.98 ± 3.92) as shown in Fig. 9a.

3.5. *Effect of Cu supercooling on the GTAW (Cu–SS) weld solidification modes*

The solidification mode evolving during fusion welding processes is generally depended on three key solidification parameters such as temperature gradient (*G*), solidification rate (*R*) and constitutional supercooling. The ratio (*G*/*R*) can predicts the condition required for various solidification modes such as planar, cellular, columnar dendritic and equiaxed dendritic solidifications. The theory behind the ratio (*G*/*R*) and constitutional supercooling for these solidification modes has been described elsewhere [26,27]. However, it is quite complicated to understand the theory behind the solidification modes involved in a typical dissimilar welded joints between the Cu and SS using

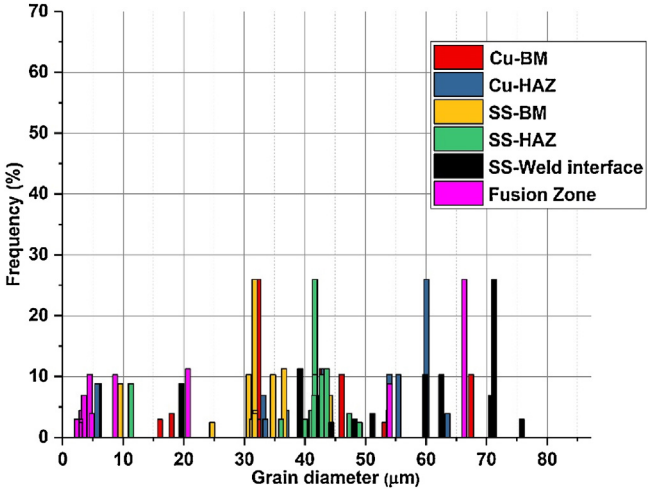

Fig. 11 – Grain size statistics of the local weld zones of the GTAW (Cu–SS) joint.

Table 5 – Average grain size and the proportion of grain boundaries across various zones of the GTAW (Cu–SS) weld.

Region	Average grain size (μm)	Proportion of HAGBs (%)	Proportion of LAGBs (%)
Cu-BM	38.47 ± 5.48	36.75	63.24
Cu-HAZ	42.99 ± 4.71	75.51	24.48
SS-BM	31.17 ± 6.03	25.87	74.12
SS-HAZ	39.20 ± 5.07	25.15	74.84
SS–weld interface	52.98 ± 3.92	53.57	46.42
Fusion zone	13.72 ± 7.47	11.36	88.63

the concept of (G/R) ratio. This is because, the G and R parameters is depended on the properties of both Cu and SS. As the Cu has very high thermal conductivity in compared to the SS, therefore Cu can dissipate significant amount of heat away from the fusion zone and it will led to constitutional supercooling effects. Hence, the solidification modes involved in the GTAW (Cu–SS) weld could be better understood through the constitutional supercooling theory in compared to evaluating the (G/R) ratio between the dissimilar metals.

Fig. 12 shows the spatial locations (1, 2, 3, and 4) of various solidification modes in the (Cu–SS) weld as determined through the optical and SEM micrographs. It is noteworthy that, the scale of constitutional supercooling is apparently increasing towards Cu due to its high thermal conductivity. The varying effects of constitutional supercooling on the solidification modes is demonstrated in Fig. 12. From this figure, it can be inferred that a very high and low cooling rates would lead to equiaxed dendritic (4) and planar solidification (1) modes respectively. The transition from the equiaxed dendritic (4) to columnar dendritic (3) solidification mode is noted in the region away from the centre line of the fusion zone. All the dendrites produced via columnar dendritic solidification mode are fully grown in compared to the fine equiaxed dendrites due to less cooling rate involved at the time of solidification. As the SS–weld interface is located further away from the fusion zone and Cu BM, apparently it has less supercooling effects from the Cu and it led to cellular solidification (2). All the above findings are exactly aligned with the constitutional supercooling theory as explained in [26]. The varying solidification rates between the dissimilar materials (Cu and SS) as well as constitutional supercooling effects received from the Cu are responsible for the range of solidification modes in the GTAW (Cu–SS) weld. Hence, the different solidification modes have led to the evolution of microstructural gradients and local property variations in the dissimilar weld.

3.6. *Tensile properties and local strain evaluations of the GTAW (Cu–SS) joint*

To evaluate the transverse tensile properties of the GTAW welds, three sub-size tensile specimens of standard dimensions

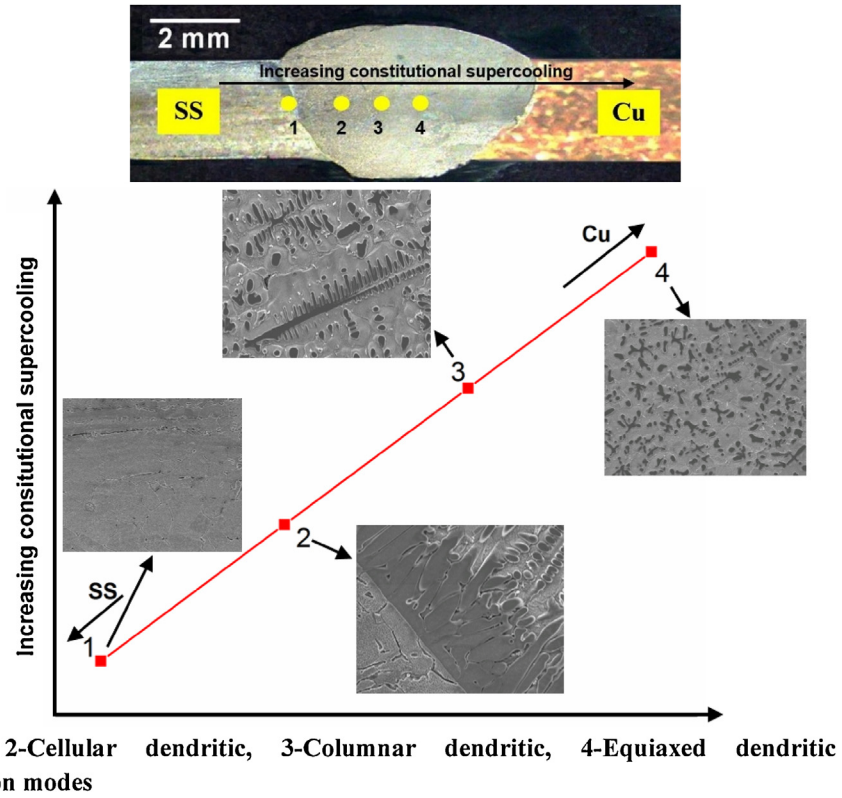

Fig. 12 – (a) Location of various solidification modes in the GTAW (Cu–SS) weld, (b) increasing constitutional supercooling vs solidification modes.

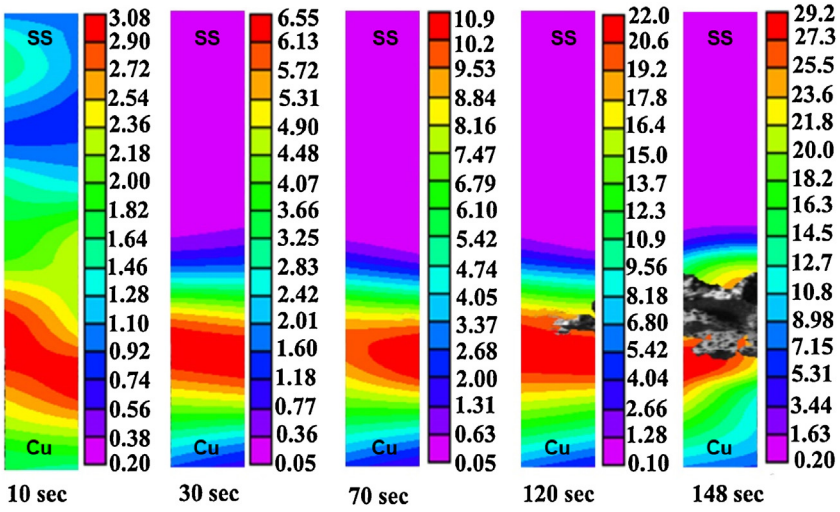

Fig. 13 – Sequential strain maps obtained through 2D-DIC.

were tested to failure and it is noticed that all the specimens have fractured in the Cu-HAZ. This clearly indicates the good compatibility between the filler material, process parameters and the dissimilar metals. Thus the sound mechanical behaviour was derived in all the traverse tensile specimens. The failure in the Cu-HAZ was apparently due to its coarse grains and also the lower hardness compared to the Cu-BM. Fig. 13 shows the progressive 2D-DIC strain maps derived from the typical GTAW (Cu–SS) joint. From these maps, it is clearly observed that initially the strain gradient in the BMs is very low and that the majority of the strain is partitioned to the Cu-HAZ and weld metal. However, as the specimen entered into the plastic deformation, the Cu-HAZ accumulates a larger quantity of strain and strain localization is evidenced. This proved that the Cu-HAZ is the weakest zone among all local weld zones of the GTAW (Cu–SS) joint. In addition to that, the weld metal get strained within 5% as the strain was localized at the Cu-HAZ and this trend continues until the specimen get fractured. Therefore, this event clearly demonstrates the sound mechanical behaviour of the weld metal compared to the Cu-BM due to the fine SS grains occupied in the fusion zone as observed in the EBSD micrographs. In compared to the Cu-BM, the scale of deformation achieved by the SS-BM is much lower due to its higher strength characteristics. These strain maps were correlated with the sequentially stitched optical micrographs in the same spatial coordinates. Hence the local weld zones (Cu-BM, Cu-HAZ, SS-HAZ and weld metal) were identified and the corresponding local DIC strains were exactly derived from these zones.

To construct the local stress–strain curves, an uniform stress condition was applied to calculate the stresses and these stresses are mapped with the local DIC strains as shown in Fig. 14. This figure shows both DIC and conventional tensile tests derived engineering stress–strain curves obtained from the local weld zones such as base metal (BM), heat affected zone (HAZ) of Cu and SS as well as the fusion zone (weld metal). In order to validate the DIC results, the longitudinal tensile specimen machined along the fusion zone (as shown in Fig. 2b) was tested to evaluate the tensile properties of the weld metal. It is clearly inferred that the stress–strain curves

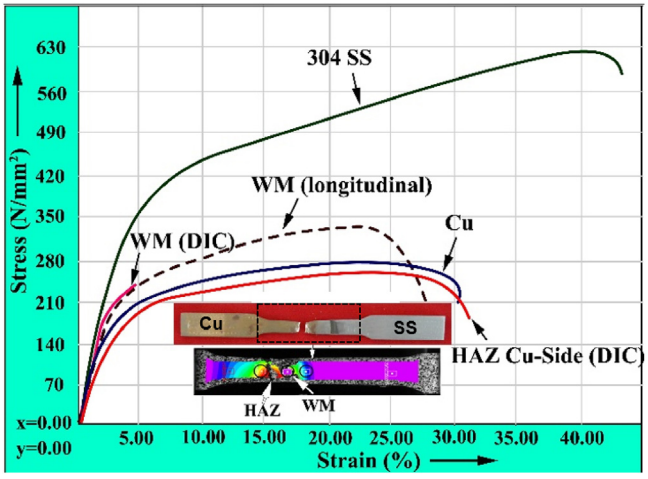

Fig. 14 – Engineering stress–strain curves of the GTAW (Cu–SS) joint.

Table 6 – Tensile properties of the base metals and welded joints.

Material	Yield strength (MPa)	Ultimate tensile strength (MPa)	% Elongation	Fracture strain
Cu	142 ± 6	280 ± 8	31.33	0.46 ± 0.05
SS	462 ± 9	630 ± 12	25.12	0.32 ± 0.05
Cu–SS joints (failure in Cu-HAZ)	181 ± 10	258 ± 14	10.65	0.30 ± 0.02
Cu–all weld metal (longitudinal)	210 ± 5	328 ± 12	9.85	0.27 ± 0.02

derived via DIC and conventional uniaxial tensile test of the weld metal are corroborating with each other. In addition to that, the local mechanical behaviour of the weld metal is closely approaching the Cu-BM. The tensile strength achieved by the weld metal (longitudinal) is determined as 328 MPa and it is found as 14.6% higher than the Cu-BM. It is noteworthy that fracture strain of the fusion zone is slightly less than the both base materials and their HAZs. This is because of the compositional gradients as observed in the EDS micrographs. The tensile strength achieved by the Cu-HAZ is 270 MPa and it

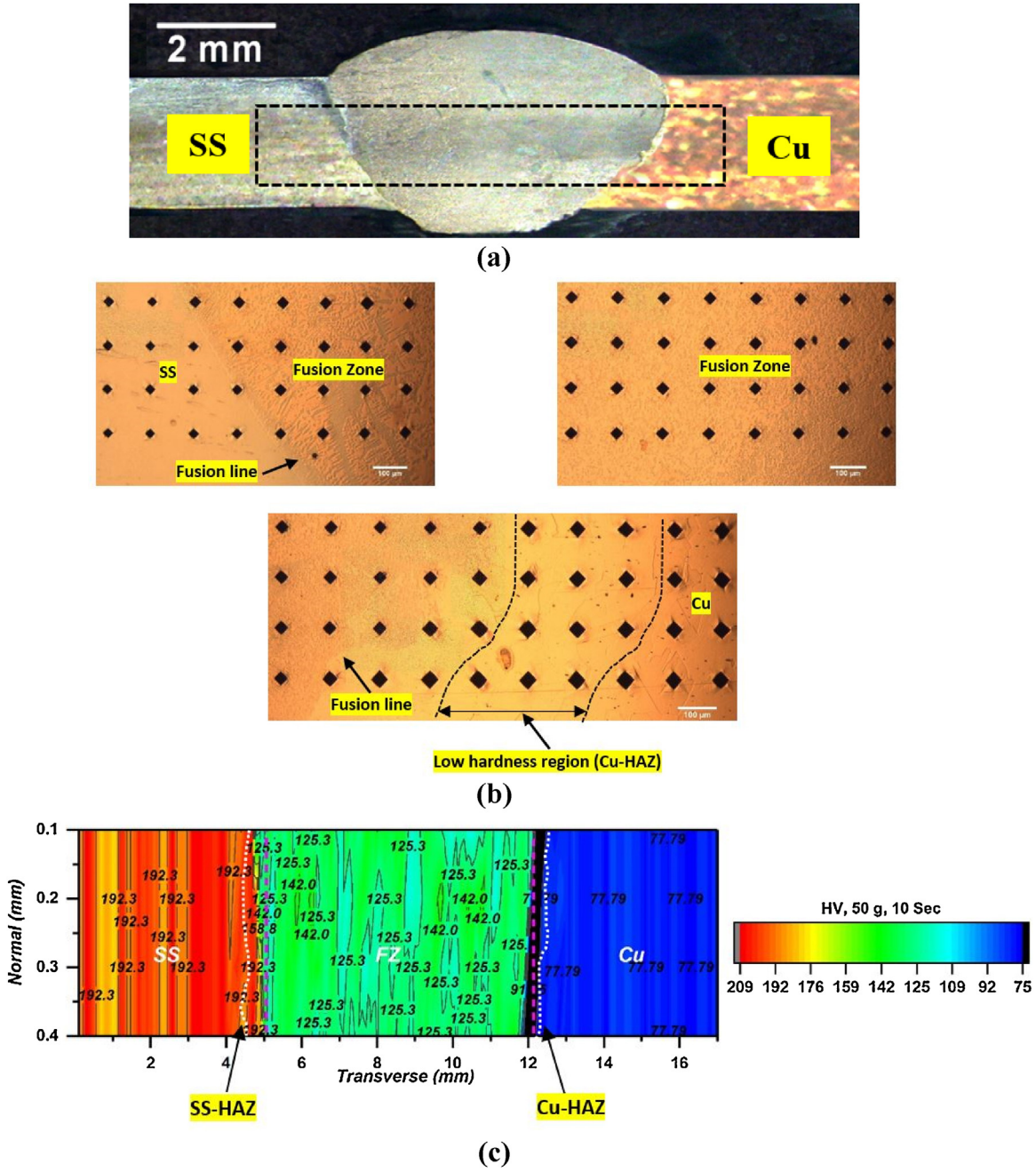

Fig. 15 – (a) ROI for hardness mapping, (b) optical micrographs showing microhardness indents, and (c) microhardness contour map along the cross-section of the weld.

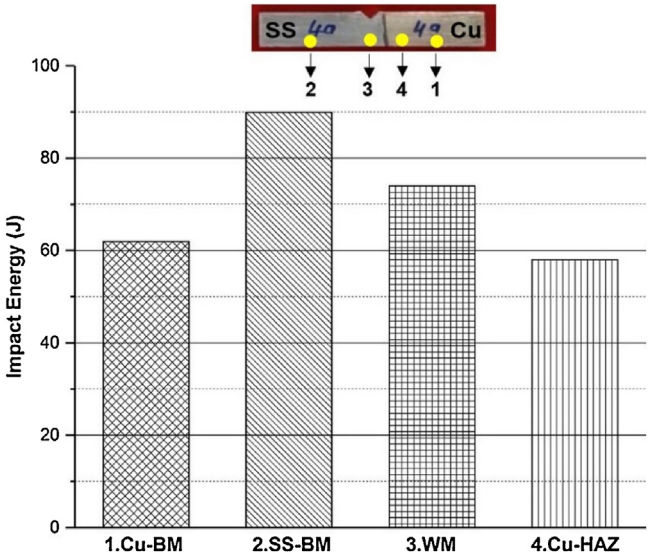

Fig. 16 – Impact toughness of the base materials and GTAW (Cu–SS) joint.

is 3.57% lower than the Cu-BM. Thus all the tensile tested (transverse) specimens were fractured in the Cu-HAZ and the joint efficiency is calculated as 92.1%.

From the tensile properties displayed in Table. 6, the average UTS and % elongation achieved by the welded joint is 258 ± 14 MPa and 10.65% respectively. The maximum tensile strength achieved in this study is almost aligned with the key investigations performed in the GTAW (Cu–SS) joints [20,21]. The UTS and elongation % achieved by the welded joint is found to be 95.55% and 33.99% of the Cu base material. The low % elongation is believed due to the minor interior defects (porosity or cracks) in the welded joint and therefore the defects can develop significantly during the tensile test which led to premature failure. Although the welded joint has comparatively less elongation % than the Cu base material, other tensile properties (tensile strength, fracture strain) achieved by the welded joint are closely associated with the Cu base material.

3.7. *Microhardness mapping*

To accurately map the microhardness distribution, a suitable area for placing the indents was identified as shown in Fig. 15a and indents were positioned in a grid spacing of 0.1 mm intervals as shown in Fig. 15b. The hardness value of these indents were individually measured and the microhardness contour map (Fig. 15c) was generated from the measured hardness values around the area that covered all the local weld zones. The hardness distributions are found to be more homogeneous in the base materials with an average hardness of 196.47 ± 8.6 HV and 80.51 ± 2.58 HV for stainless steel and copper respectively. A high standard deviation in the SS-BM is due to presence of δ-Ferrite in the austenite matrix as confirmed in the optical micrographs. The hardness achieved by the indents exclusively positioned on the delta ferrite phase is varying from 184.6 HV to 208.9 HV. It is noteworthy that, the highest hardness (208.9 HV) is recorded in the delta ferrite region as the ferrite phase is generally harder than the austenite (γ-Fe) due to its high chromium content (Ferrite stabilizer). This same trend was also observed by Mortazavi et al. [31]. A dip in the hardness values is observed both in the SS and Cu HAZs as these zones were affected by the heat. The fusion zone has a sharp fluctuation in the hardness values (111.5–148.5 HV) with the average hardness value of 129.28 ± 19.22 HV. This is because of the significant presence of columnar dendrites (Fe) within the copper matrix (Cu). The high hardness gradients of the fusion zone is also interlinked with the local compositional and temperature gradients achieved during the weld solidification as mentioned elsewhere [10–12]. Thus the fusion zone has less hardness compared to the SS-BM. The hardness transition from the fusion zone to SS–weld interface is more gradual, however due to much coarse Cu grains, the hardness depletion region is clearly noticed for a few hundred microns along the Cu–weld interface (Fig. 15b). All these findings are in line with the metallurgical findings obtained from the SEM and SEM-EDS.

3.8. *Impact toughness*

Impact specimens with V-Notch at the weld centre and also at the Cu-HAZ have subjected to Charpy impact toughness test at room temperature and the average recorded values of these specimens are shown in Fig. 16. From this figure, it is inferred that the weld joint is tougher than the weaker base metal (i.e., Cu). This is because, the GTAW (Cu–SS) joint has achieved a superior impact properties received from both dissimilar materials (Cu and SS) compared to the Cu-BM. Impact toughness specimens with the notch located at the weld centre have absorbed 21.62% higher energy compared to Cu-BM. However, the specimen which has the notch at the Cu-HAZ has experienced lower impact toughness compared to the notch at the weld centre. It is noted that all the impact specimens were fractured in the region very close to the Cu-HAZ. All the aforementioned findings confirm the high impact toughness characteristics of the weld metal compared to the Cu-HAZ.

4. Conclusions

The effect of GTA welding process on the Cu–SS joints using ERNiCu-7 filler material was investigated through the detailed insight into the material characterizations of the GTAW (Cu–SS) welds. The vital conclusions derived from this investigation are as follows:

- The GTA welded (Cu–SS) joint using ERNiCu-7 filler material with the optimized process parameters produced a sound dissimilar material joints without any major weld defects in the fusion zone and also in the weld interfaces. All the optical and SEM micrographs agree these findings. Therefore, ERNiCu-7 filler material could be preferred as an appropriate filler material for joining the copper to stainless steel.
- Weld metal has rich mixture of columnar and equiaxed dendrites. Additionally, the centre of the fusion zone exhibits the hybrid microstructure containing significant amount of fine steel globules randomly distributed on the copper matrix. Epitaxial grain growth with delta ferrites (BCC) are evidenced along the SS interface.
- Energy Dispersive Spectroscopy (EDS) performed under SEM-BSE mode clearly revealed the compositional gradients across the weld in compared to the SEM-SEI. Electron Back Scattered Diffraction (EBSD) results confirmed the distribution of dense fine grains in the fusion zone resulted from the dendritic solidification and coarse grains along the SS-interface.
- From the 2D-DIC analysis, the local stress–strain curves of the weld metal and HAZs are derived. The stress–strain curve of the weld metal is very close to Cu-BM and the weld metal has achieved the tensile strength equivalent to the Cu-BM. Major DIC findings are aligned with the results derived from the conventional uniaxial tensile tests performed on the transverse and longitudinal tensile specimens. All the tensile specimens were fractured in the Cu-HAZ due to its low hardness and very coarse copper grains.
- Microhardness gradients are observed across the fusion zone due to the heterogeneous distribution of Cu and SS grains. Even though the fusion zone had more fine SS globules, the average microhardness achieved by the fusion zone is considerably lower than the SS-BM. The lowest hardness was found in the Cu-HAZ.
- Hence, the GTA welded C21000 to Cu-304 stainless steel joint manufactured with ErNiCu-7 filler material has the ability to serve the applications elsewhere with sound properties wherever both high thermal conductivity and corrosion resistance are required.

Conflict of interest

None declared.

Ethical statement

This paper is an original work and has been neither published nor submitted for publication elsewhere.

Acknowledgement

The authors wish to place their sincere thanks to SSN Trust for the support through students internal funding to carryout this research and the Director, IGCAR for extending Digital Image Correlation (DIC) Facility.

REFERENCES

[1] N. Kumar, R.S. Mishra, Friction Stir Welding of Dissimilar Alloys and Materials, Elsevier Publication, 2015.
[2] B. Silwal, L. Li, A. Deceuster, B. Griffiths, Effect of post weld heat treatment on the toughness of heat-affected zone for grade 91 steel, Weld. J. 92 (2013) 80–87.
[3] C. Pandey, M.M. Mahapatra, P. Kumar, N. Saini, Homogenization of P91 weldments using varying normalizing and tempering treatment, Mater. Sci. Eng. A 710 (2018) 86–101.
[4] J. Cao, Y. Gong, K. Zhu, Z.G. Yang, X.M. Luo, F.M. Gu, Microstructure and mechanical properties of dissimilar materials joints between T92 martensitic and S304H austenitic steels, Mater. Des. 32 (5) (2011) 2763–2770.
[5] K. Martinsen, S.J. Hu, B.E. Carlson, Joining of dissimilar materials, CIRP Ann. Manuf. Technol. 64 (2) (2015) 679–699.
[6] A.J. Ramirez, D.M. Benati, Effect of tool offset on dissimilar Cu-AISI 316 stainless steel friction stir welding, in: Proc. 21st International Offshore and Polar Engineering Conference, 2011.
[7] C. Lusch, M. Borsch, C. Heidt, N. Magginetti, J. Sas, K.P. Weiss, Qualification of electron-beam welded joints between copper and stainless steel for cryogenic application, in: IOP Conference Series, 2015.
[8] T.A. Mai, A.C. Spowage, Characterisation of dissimilar joints in laser welding of steel–kovar, copper–steel and copper–aluminium, Mater. Sci. Eng. A 374 (1–2) (2004) 224–233.
[9] I. Magnabosco, P. Ferro, F. Bonollo, L. Arnberg, An investigation of fusion zone microstructures in electron beam welding of copper–stainless steel, Mater. Sci. Eng. A 424 (1–2) (2006) 163–173.
[10] J. Kar, S.K. Roy, G.G. Roy, Effect of beam oscillation on electron beam welding of copper with AISI-304 stainless steel, J. Mater. Process. Technol. 233 (2016) 174–185.
[11] S. Chen, J. Huang, J. Xia, H. Zhang, X. Zhao, Microstructural characteristics of a stainless steel/copper dissimilar joint made by laser welding, Metal. Mater. Trans. A 44 (8) (2013) 3690–3696.
[12] C. Yao, B. Xu, X. Zhang, J. Huang, J. Fu, Y. Wu, Interface microstructure and mechanical properties of laser welding copper–steel dissimilar joint, Opt. Laser. Eng. 47 (7–8) (2009) 807–814.
[13] G. Phanikumar, S. Manjini, P. Dutta, K. Chattopadhyay, J. Mazumder, Characterization of a continuous CO2 laser-welded Fe–Cu dissimilar couple, Metal. Mater. Trans. A 36 (8) (2005) 2137–2147.
[14] A. Durgutlu, B. Gülenç, F. Findik, Examination of copper/stainless steel joints formed by explosive welding, Mater. Des. 26 (6) (2005) 497–507.
[15] A. Durgutlu, H. Okuyucu, B. Gulenc, Investigation of effect of the stand-off distance on interface characteristics of explosively welded copper and stainless steel, Mater. Des. 29 (7) (2008) 1480–1484.
[16] V. Shokri, A. Sadeghi, M.H. Sadeghi, Effect of friction stir welding parameters on microstructure and mechanical

properties of DSS–Cu joints, Mater. Sci. Eng. A 693 (2017) 111–120.
[17] Y. Imani, G. Besharati, M.K. Guillot, Improving friction stir welding between copper and 304L stainless steel, Adv. Mater. Res. 409 (2011) 263–268.
[18] T. Wang, S. Shukla, S.S. Nene, M. Frank, R.W. Wheeler, R.S. Mishra, Towards obtaining sound butt joint between metallurgically immiscible pure Cu and stainless steel through friction stir welding, Metal. Mater. Trans. A 49 (7) (2018) 2578–2582.
[19] C. Leitão, I. Galvão, R.M. Leal, D.M. Rodrigues, Determination of local constitutive properties of aluminium friction stir welds using digital image correlation, Mater. Des. 33 (2012) 69–74.
[20] S.G. Shiri, M. Nazarzadeh, M. Sharifitabar, M.S. Afarani, Gas tungsten arc welding of CP-copper to 304 stainless steel using different filler materials, Trans. Nonferrous Metals Soc. China 22 (12) (2012) 2937–2942.
[21] C.C. Chang, L.H. Wu, C. Shueh, C.K. Chan, I.C. Shen, C.K. Kuan, Evaluation of microstructure and mechanical properties of dissimilar welding of copper alloy and stainless steel, Int. J. Adv. Manuf. Technol. 91 (5) (2017) 2217–2224.
[22] M. Velu, S. Bhat, Metallurgical and mechanical examinations of steel–copper joints arc welded using bronze and nickel-base superalloy filler materials, Mater. Des. 47 (2013) 793–809.
[23] ASTM E8/E8M-16a, Standard Test Methods for Tension Testing of Metallic Materials, ASTM International, 2016.
[24] ASTM E23-12c, Standard Test Methods for Notched Bar Impact Testing of Metallic Materials, ASTM International, 2012.
[25] ASTM E384-17, Standard Test Method for Microindentation Hardness of Materials, ASTM International, 2017.
[26] S. Kou, Welding Metallurgy, 2nd ed., John Wiley & Sons, 2003.
[27] J.C. Lippold, Welding Metallurgy and Weldability, John Wiley & Sons, 2014.
[29] H. Chen, L. Fu, P. Liang, Microstructure, texture and mechanical properties of friction stir welded butt joints of 2A97 AlLi alloy ultra-thin sheets, J. Alloys Compd. 692 (2017) 155–169.
[30] S. Cui, Y. Shi, K. Sun, S. Gu, Microstructure evolution and mechanical properties of keyhole deep penetration TIG welds of S32101 duplex stainless steel, Mater. Sci. Eng. A 709 (2018) 214–222.
[31] E. Mortazavi, R.A. Najafabadi, A. Meysami, Effect of heat input on microstructure and mechanical properties of dissimilar joints of AISI 316L steel and API X70 high-strength low-alloy steel, J. Iron Steel Res. Int. 24 (12) (2017) 1248–1253.